Influence of alloy element distributions on austempered ductile irons

A. D. Boccardo, P. M. Dardati & L. A. Godoy

Published online: 19 Sep 2018.

Submit your article to this journal ↗

View Crossmark data ↗

Iom³

The Institute of Materials,
Minerals and Mining

Taylor & Francis
Taylor & Francis Group

Check for updates

Influence of alloy element distributions on austempered ductile irons

A. D. Boccardo [a,b], P. M. Dardati [b] and L. A. Godoy [a,c]

aInstituto de Estudios Avanzados en Ingeniería y Tecnología, IDIT, CONICET-Universidad Nacional de Córdoba, Córdoba, Argentina; bGrupo de Investigación y Desarrollo en Mecánica Aplicada, GIDMA, Facultad Regional Córdoba, Universidad Tecnológica Nacional, Córdoba, Argentina; cFacultad de Ciencias Exactas, Físicas y Naturales, Universidad Nacional de Córdoba, Córdoba, Argentina

ABSTRACT

The influence of alloy element distributions on austempered ductile iron microstructure and austempering treatment was analysed by a cellular automaton model that considers the ausferritic and martensitic transformations. The initial microstructure is modelled as spherical graphite nodules inserted in an austenitic matrix, in which the alloy elements are distributed in a uniform or non-uniform way. The study is performed for different chemical compositions and graphite nodule sizes. Delays in the development of ausferritic transformation are produced by the increment of graphite nodule size and the presence of alloy element microsegregations. Moreover, microsegregation reduces the final volume fraction of ferrite platelets. The predicted retained austenite volume fraction is in good agreement with the experimental measurements reported in the literature.

Introduction

Austempered ductile iron (ADI) is an Fe–C–Si alloy, whose microstructure is formed by graphite nodules inserted in an ausferritic matrix. At ambient temperature, this matrix is commonly constituted by austenite blocks and sheaves formed by ferrite platelets and austenite films [1, 2].

The ADI microstructure is frequently obtained by a three-step austempering heat treatment. In the first step, the ductile iron is austenitised at the temperature of 1123 K (850°C)$< T_\gamma <$1223 K (950° C). During the second step, it is cooled and kept at the austempering temperature [523 K (250°C)$< T_A <$723 K (450° C)]. Finally, in the third step, the material is cooled down to ambient temperature [3]. During the second step of the heat treatment, the ausferritic transformation, also known as stage I reaction, takes place. In this reaction, austenite transforms into ferrite platelets by means of the displacive growth mechanism that involves continuous processes of ferrite nucleation, ferrite platelet growth without carbon diffusion, and carbon rejection from carbon-supersaturated ferrite to austenite [1, 4]. During the third step, austenite may transform into martensite by means of the martensitic transformation [5].

For ADI parts, especially for those formed by thick sections, alloy elements such as Mo, Mn, Si, Cu, and Ni are added to increase the hardenability, which allows to avoid the formation of ferrite and pearlite during the cooling down from austenitising temperature to austempering temperature [6]. The alloy elements segregate in two different ways: (a) positive segregation, in which elements are concentrated at last to freeze (LTF) region (Mo and Mn) and (b) negative segregation, in which elements are concentrated at first to freeze (FTF) region (Si, Cu, and Ni) [6, 7]. Mo and Mn are employed as potent hardenability agents but they delay the formation of ferrite platelets, especially at the intercellular boundaries where these elements strongly segregate [7–9]. Ni and Cu are also employed to increase the hardenability. They have the advantage of producing less microsegregations but also delay the ferrite platelets formation [10].

The microsegregated alloy elements may form carbide during solidification, and also generate different hardenabilities and transformation rates in the matrix that may cause difficulties in controlling the austempering heat treatment process [6]. The severe alloy element microsegregations are reduced by increasing the graphite nodule count [6, 7, 11], which allows to decrease the continuity of the unreacted intercellular boundary [7]. Moreover, the increment of graphite nodule count increases the interface area between nodules and matrix, which increases the transformation rate [3]. Other technique that has been employed to reduce the microsegregations of Mo and Mn, in parts with thick sections, is the partial melting homogenisation [12, 13].

For the reasons mentioned above, it is important to predict the influence of microsegregations on the ADI

microstructure and the austempering heat treatment. In the literature review, a few models were found concerning the simulation of the ausferritic transformation in ductile iron. Although geometrical characteristics of ADI microstructure have been taken into account by several models, in most of them the microsegregations of alloy elements were not considered [14–17]. The model proposed by Thomson et al. [4] considers the microsegregation effect on ADI taking into account a rectangular distribution of graphite nodules within the matrix. The austenite volume located between a graphite nodule and the halfway between this nodule and a neighbouring nodule is divided into shells; and a homogeneous chemical composition is computed in each shell by means of Scheil equation [18]. For each shell, the phase change model was employed to compute the austenite carbon concentration (at the beginning and at the end of the transformation), the initial driving force to transform austenite, the phase evolution, and the final volume fraction of ferrite platelets [4, 19]. Because the analysis was performed for each shell, it is not simple to assess the overall microsegregation effects on the ADI microstructure and the heat treatment.

This work studies the influence of homogeneous and microsegregated distributions of alloy elements on ADI and its heat treatment. The investigation is conducted numerically using a 3D cellular automaton-finite difference (CA-FD) model previously implemented by the authors for a homogeneous distribution (HD) of alloy elements [17], which is modified in this work to consider the microsegregation of alloy elements. The microsegregated distribution is obtained by employing the Scheil equation, which generates a severe microsegregation pattern.

CA-FD model

This section presents a description of the CA-FD model employed to simulate the phase changes that occur during the second and third steps of the austempering heat treatment of a ductile iron. The model takes into account the size and distribution of graphite nodules, the alloy element distributions in austenite, the size of ferrite platelets, the interaction between growing sheaves, and the carbon diffusion within the matrix during the ausferritic transformation. In this model, the 3D domain is uniformly divided into an orthogonal arrangement of cubic cells with side length identified as cd.

Initial microstructure

The initial microstructure of ductile iron is formed by graphite nodules embedded in a full austenitic matrix, i.e. it is considered that there is no carbide formation during the solidification of the material.

The micro-constituent features are introduced in the model through the digital material representation method [20].

For this analysis, a cubic shape domain (Ω_{cube}) with a periodic geometry is employed, in which the graphite nodules are modelled as spheres of equal size. The dimension of the cubic domain is chosen to include the graphite nodules and to satisfy a graphite volume fraction that ranges between $0.05 \leq f_{\text{Gr}} \leq 0.15$ (dilute case). A random, statistically homogeneous, and isotropic spatial distribution of nodules in the domain is performed by the random sequential addition process [21]. The volume fraction of graphite nodules can be obtained from experimental tests or from models that take into account the mass conservation of alloy elements. The centre coordinates of non-overlapping nodules are obtained with a uniform pseudo-random number generator. The carbon concentration of graphite nodules is assumed to be homogeneous and equal to $c_{\text{Gr}} = 100$ in weight per cent (wt- %) [16].

At the beginning of the simulation, the carbon content is homogeneously distributed in the austenite. The carbon content of each austenite cell depends on the austenitising temperature (temperature of the first step of the austempering heat treatment) and the nominal content of alloy elements in austenite. The initial austenite carbon concentration, in wt-%, is computed using the following expression [2]:

$$
\begin{aligned}
W_{\text{C}\gamma} = {} & 0.335 \times 10^{-3}(T_\gamma - 273) + 1.61 \\
& \times 10^{-6}(T_\gamma - 273)^2 + 0.006 W_{\text{Mn}_n} - 0.11 W_{\text{Si}_n} \\
& - 0.07 W_{\text{Ni}_n} + 0.014 W_{\text{Cu}_n} - 0.3 W_{\text{Mo}_n} - 0.435
\end{aligned}
\tag{1}
$$

where W_{i_n} is the nominal concentration of alloy element i in austenite in wt-% and T_γ is given in K.

The nominal concentration of alloy elements in austenite is higher than the nominal chemical composition of the ductile iron, because the graphite nodules are formed only by carbon. The nominal concentration of each alloy element i is computed with the following equation [22]:

$$
W_{i_n} = W_{i_o}\left(\frac{\rho_{\text{Gr}}f_{\text{Gr}} + \rho_\gamma f_{\gamma_o}}{\rho_\gamma f_{\gamma_o}}\right)
\tag{2}
$$

where W_{i_o} is the nominal concentration of element i in the ductile iron, f_{Gr} and f_{γ_o} are the volume fractions of graphite nodules and austenite, and $\rho_{\text{Gr}} = 2200$ kg m^{-3} and $\rho_\gamma = 7900$ kg m^{-3} are the graphite and austenite densities [22], respectively.

HD of alloy elements

For HD of alloy elements in austenite, the concentration of alloy element i for each austenite cell is computed with Equation (2) ($W_i = W_{i_n}$).

Microsegregated distribution of alloy elements

The non-uniform distribution of alloy elements in the austenite is obtained by modelling the solidification process of the material. It is considered that ductile iron solidifies according to the uninodular solidification theory, in which austenite halos grow from the graphite nodule surfaces [22]. The alloy element distributions are computed with the Scheil equation that considers local equilibrium at solid-liquid interface, no diffusion of alloy elements in the solid, and perfect mixing of alloy elements in the liquid. The Scheil equation produces a severe microsegregation pattern in comparison with the model of Ref. [23] that considers limited diffusion of alloy elements at liquid and solid phases.

In order to compute the microsegregation pattern, first, the graphite nodules are placed into the cubic domain. Then, austenite halos grow until the matrix is completely austenitic. During the growth of halos, the alloy element concentrations for each austenite cell are computed by the Scheil equation as follows:

$$W_i = k_i W_{i_n} (1 - f_{\gamma sol_n})^{(k_i - 1)} \tag{3}$$

where k_i is the equilibrium segregation coefficient of the alloy element i and $f_{\gamma sol_n} = f_{\gamma sol}/(1 - f_{Gr})$ is the austenite volume fraction during the solidification process normalised with respect to the matrix volume fraction.

The austenite volume fraction during the solidification process is computed as follows:

$$f_{\gamma sol} = \frac{nc_{\gamma sol}}{nc} \tag{4}$$

where $nc_{\gamma sol}$ is the number of cells with austenite halo state and nc is the total number of cells.

Phase evolution

The phase evolution during the second and third steps of the austempering heat treatment, due to the development of ausferritic and martensitic transformations respectively, are modelled by means of a CA-FD model. It is based on a model previously presented by the authors [17] and a brief description of it is presented below.

Ausferritic transformation

As stated by the displacive growth mechanism, austenite transforms into ferrite platelets when the thermodynamic criteria for nucleation ($\Delta Gm < Gn$) and growth ($\Delta G^{\gamma \to \alpha} < G_{sd}$) are satisfied [24], where ΔGm is the maximum free energy available for paraequilibrium nucleation, Gn is the minimum energy necessary to obtain a detectable amount of ferrite, $\Delta G^{\gamma \to \alpha}$ is the free energy change for the transformation of austenite into ferrite, and G_{sd} is the stored energy due to the shape deformation. The increment of austenite carbon concentration modifies the magnitudes of ΔGm and $\Delta G^{\gamma \to \alpha}$. When the austenite carbon concentration

reaches the value $W_{C_{\gamma_{To'}}}$, either one or both thermodynamic criteria are not satisfied and the ausferritic transformation stops.

The micro-constituents considered in the model are graphite nodules, austenite blocks, and sheaves. A sheaf is formed by a fix relation of ferrite platelets and austenite films, and it is modelled as an octagonal bipyramid, see Figure 1. The pyramid height is $l_{sh} = n_h l_{\alpha p}$, where n_h is the maximum number of ferrite platelets in the height direction and $l_{\alpha p}$ is the length of a ferrite platelet. The circumradius of the pyramid base is $r_{sh} = n_r(t_{\alpha p} + t_{\gamma f})$, where n_r is the number of ferrite platelets in the base in the radial direction, and $t_{\alpha p}$ and $t_{\gamma f}$ are the thicknesses of a ferrite platelet and an austenite film, respectively.

Sheaf nucleation: At the beginning of the simulation, each austenite cell is set with an uncaptured state. The phase transformation starts with the nucleation of sheaves in austenite cells placed at nodule-austenite interfaces. When the nucleation occurs in an austenite cell, this cell is set as captured and when the bipyramid starts to grow it is set as a sheaf. The nucleation of each sheaf is performed as Figure 2 illustrates, in which the questions are Q1: Is the austenite cell in an uncaptured state?; and Q2: Is the carbon concentration of the austenite cell lower than $W_{C_{\gamma_{To'}}}$?. The orientation angles θ and φ of each sheaf with respect to the domain coordinate system xyz, shown in Figure 1, are randomly assigned.

The following continuous nucleation rate law is employed for sheaves nucleation:

$$\dot{N}_{nai} = \frac{N_{nai}^{max}}{t_{inc}} \tag{5}$$

where $\dot{N}_{nai}$ is the number of austenite cells placed at nodule-austenite interfaces, per unit of time, in which sheaves are nucleated, N_{nai}^{max} is the maximum number of austenite cells in which sheaves are able to nucleate, and t_{inc} is the incubation time of a ferrite platelet.
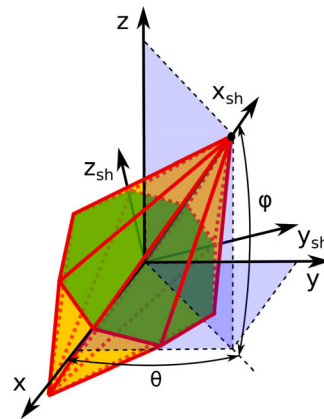

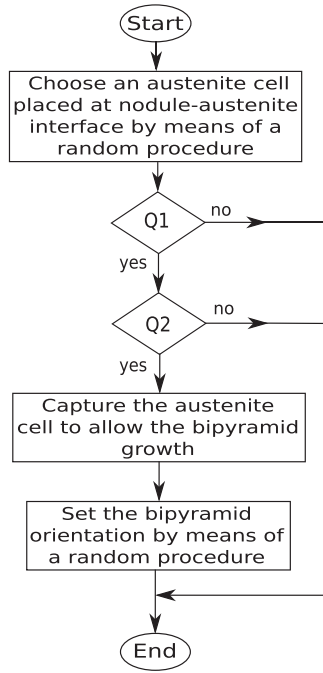**Figure 1.** Bipyramid employed to represent the sheaf geometry.

Figure 2. Flow diagram for the nucleation of a sheaf in an austenite cell placed at the nodule-austenite interface.

The maximum number of austenite cells in which sheaves are able to nucleate is calculated as $N_{\text{nai}}^{\max} = (f_{\alpha p}^{\max} l_{\alpha p} s_{\text{Gr}})/u_{\alpha p}$, where $f_{\alpha p}^{\max}$ is the maximum volume fraction of ferrite platelets that can be formed within an ausferrite halo (placed around a graphite nodule and with external radius $r_{\text{Gr}} + l_{\alpha p}$) with respect to the halo volume fraction when the transformation time is equal to t_{inc}, s_{Gr} is the total surface of graphite nodules, and $u_{\alpha p}$ is the volume of a ferrite platelet. According to Ref. [25], the ferrite platelet length, in m, and volume, in m^3, are $l_{\alpha p} = 1 \times 10^{-5}(T_A - 528)/150$ and $u_{\alpha p} = 2 \times 10^{-17}[(T_A - 528)/150]^3$, respectively. The maximum volume fraction of ferrite platelets is computed as follows [5]:

$$f_{\alpha p}^{\max} = \frac{W_{C_{\gamma_{To'}}} - W_{C_\gamma}}{W_{C_{\gamma_{To'}}} - W_{C_{\alpha p}}} \tag{6}$$

where $W_{C_{\alpha p}}$ is the ferrite platelet carbon concentration, which is set as $W_{C_{\alpha p}} = 0.03$ wt-% [5]. The austenite carbon concentration $W_{C_{\gamma_{To'}}}$ is calculated for each austenite cell, in wt-%, as follows [2]:

$$W_{C_{\gamma_{To'}}} = 3.072 - 0.0016(T_A - 273) - 0.24W_{Si}$$
$$- 0.161W_{Mn} - 0.115W_{Ni} + 0.25W_{Cu}$$
$$+ 0.06W_{Mo} + 2.69W_{Cr} \tag{7}$$

where W_i is the concentration of alloy element i in austenite in wt-% and T_A is given in K.

The incubation time of a ferrite platelet, in s, is calculated with Equation (8) that is based on the work of Gaude and Jacques [26]. The previously employed expression to compute t_{inc}, based on the work of Matsuda and Bhadeshia [25], was changed in order to improve the results:

$$t_{\text{inc}} = \frac{k_a}{\nu \tanh\left(-\frac{\Delta Gm - Gn}{RT_A}\right)} \tag{8}$$

where ν is the attempt frequency factor defined as $\nu = k_b T_A/h$ with k_b and h being the Boltzmann and Planck constants, respectively. Moreover, R is the universal gas constant and k_a is a constant to be fitted. This expression is employed if the thermodynamic criterion for the nucleation of ferrite platelets is satisfied. ΔGm is evaluated taking into account the alloy element concentrations of each austenite cell using the parallel tangent construction described in Ref. [27] and Gn is calculated as in Ref. [25].

Sheaf growth: The sheaf growth occurs by the formation of ferrite platelets within it, which involves the processes of autocatalytic nucleation and growth. Taking into account that the growth time of a ferrite platelet is shorter than its incubation time [25], the growth rate of the length (pyramid height) and radius (pyramid circumradius) of a sheaf are computed, respectively, as follows:

$$\dot{l}_{\text{sh}} = l_{\alpha p}/t_{\text{inc}} \tag{9}$$

$$\dot{r}_{\text{sh}} = (t_{\alpha p} + t_{\gamma f})/t_{\text{inc}} \tag{10}$$

According to the geometrical description of a ferrite platelet presented in Ref. [25], the thickness of a ferrite platelet is adopted as $t_{\alpha p} = l_{\alpha p}/10$. If the ratio of austenite film and ferrite platelet volume fractions is considered as $f_{\gamma f}/f_{\alpha p} = 0.12$ [16], the thickness of an austenite film is $t_{\gamma f} = 0.12t_{\alpha p}$.

To allow the sheaf growth in the cubic domain, the next capture algorithm is employed. The sheaf starts growing with a certain orientation in the centre of an austenite cell placed at the nodule-austenite interface. When a corner of the octagonal bipyramid touches an austenite cell placed in the Moore neighbourhood, this austenite cell is captured and a new octagonal bipyramid starts growing within it. The bipyramid in the captured cell has the same orientation as the bipyramid of the captor cell, but the growth rate occurs according to its alloy element concentrations. The flow diagram of Figure 3 illustrates the procedure employed for the capture of each austenite cell, in which the questions are Q1: Is the austenite cell in an uncaptured state?; Q2: Is the carbon concentration of the austenite cell lower than $W_{C_{\gamma_{To'}}}$?; and Q3: Is the austenite cell touched for some bipyramid that is growing in a sheaf cell placed at the Moore neighbourhood?.

The volume fractions of graphite nodules (f_{Gr}), sheaves (f_{sh}), and austenite blocks ($f_{\gamma b}$) are calculated
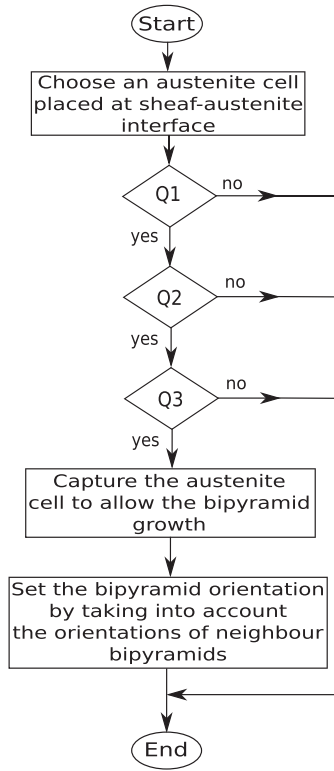
Figure 3. Flow diagram of the capture process of an austenite cell placed at the sheaf-austenite interface.

as follows:

$$f_i = \frac{\mathrm{nc}_i}{\mathrm{nc}} \qquad (11)$$

where nc_i is the number of cells with state i = graphite, sheaf, and austenite block.

Taking into account the mentioned relation between $f_{\alpha p}$ and $f_{\gamma f}$, the volume fractions of ferrite platelets ($f_{\alpha p}$) and austenite films ($f_{\gamma f}$) are computed as

$$f_{\alpha p} = 0.89286 f_{\mathrm{sh}} \qquad (12)$$

$$f_{\gamma f} = 0.10714 f_{\mathrm{sh}} \qquad (13)$$

Carbon distribution: After the growth of a carbon-supersaturated ferrite platelet within a sheaf, part of the ferrite carbon is incorporated in the austenite films (placed within the sheaf) and the remaining part is instantaneously rejected to the austenite blocks (placed next to the sheaf). Then, the received carbon is diffused in the austenite blocks.

During the rejection, the increment of carbon concentration of an austenite block cell, placed at the sheaf-austenite interface, is calculated as follows:

$$\Delta W_{C_\gamma} = \sum_{i=1}^{k} \left[\Delta fn_{sh_i} \frac{(W_{C_{\gamma_i}^{\mathrm{cap}}} - W_{C_{\mathrm{sh}}})}{\mathrm{nc}_{\gamma_i}} \right] \qquad (14)$$

where $\Delta fn_{\mathrm{sh}_i}$ is the increment of sheaf volume fraction with respect to the cell volume fraction, $W_{C_{\gamma_i}^{\mathrm{cap}}}$ is the austenite carbon concentration when the growing sheaf

cell was captured, $W_{C_{\mathrm{sh}}}$ is the sheaf carbon concentration, nc_{γ_i} is the number of austenite cells placed at the Moore neighbourhood of sheaf cell i that are able to receive carbon ($W_{C_\gamma} < W_{C_{\gamma_{To'}}}$), and k is the number of sheaf cells placed in the Moore neighbourhood of the austenite block cell.

Once the carbon rejection from sheaves to austenite blocks was performed, the carbon diffusion within the austenite block domains (Ω_γ) is calculated by employing the Fick's second law:

$$\frac{\partial W_{C\gamma}}{\partial t} = \mathrm{div}[\mathbf{D}_\gamma \, \mathrm{grad}(W_{C\gamma})] \qquad (15)$$

which is valid in $\Omega_\gamma \times \Upsilon$, where Υ denotes the time interval of interest (with time $t \in \Upsilon$). Moreover, $\mathbf{D}_\gamma$ is the isotropic carbon diffusion tensor of second-rank defined as $\mathbf{D}_\gamma = D_\gamma \mathbf{1}$, D_γ is the coefficient of carbon diffusion in austenite, and $\mathbf{1}$ is the unit tensor of second-rank. The coefficient of carbon diffusion depends on both austempering temperature and austenite carbon concentration, and it is calculated with the mathematical expression proposed by Ågren [28].

Equation (15) is solved by taking into account the following boundary conditions: (a) periodic condition at the cube boundary formed by austenite block ($\Gamma_{\mathrm{cube}_\gamma}$) and (b) carbon flux equal to zero at austenite block-graphite ($\Gamma_{\gamma_{\mathrm{Gr}}}$) and austenite block-sheaf ($\Gamma_{\gamma_{\mathrm{sh}}}$) boundaries.

Martensitic transformation

The model considers that only austenite block cells are able to transform into martensite at the end of third step of the austempering heat treatment, because the carbon concentration of austenite films is high enough to get $T_{\mathrm{MS}} < T_{\mathrm{amb}}$, where T_{MS} is the martensite start temperature and T_{amb} is the ambient temperature. The martensite volume fraction formed at ambient temperature in each austenite block cell ($f_{m_{\mathrm{cell}}}$), with respect to the cell volume fraction, is computed with the expression proposed by Khan and Bhadeshia [29]:

$$f_{m_{\mathrm{cell}}} = 1 - \exp\{-f_{m_{\mathrm{cell}}}[1 + k_{\mathrm{m}}(T_{\mathrm{MS}} - T_{\mathrm{amb}})]\} \quad (16)$$

where k_{m} is a constant to be fitted.

For each austenite block cell, the temperature T_{MS} is computed, in K, with the next equation from Ref. [30]:

$$\begin{aligned} T_{\mathrm{MS}} = 772 &- 300 W_{C_\gamma} - 33.3 W_{\mathrm{Mn}} - 11.1 W_{\mathrm{Si}} \\ &- 22.2 W_{\mathrm{Cr}} - 16.7 W_{\mathrm{Ni}} - 11.1 W_{\mathrm{Mo}} \qquad (17) \end{aligned}$$

where W_i is the concentration of alloy element i in austenite, in wt-%.

The volume fractions of martensite (f_{m}) and retained austenite ($f_{\gamma\mathrm{ret}}$), at ambient temperature, are computed
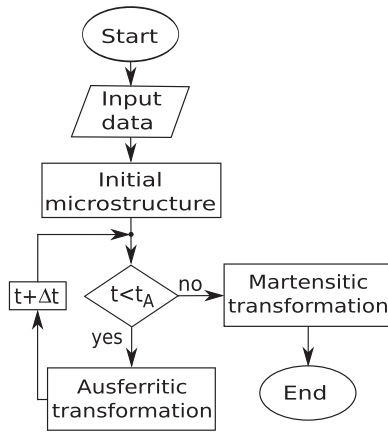
Figure 4. Flow diagram of the CA-FD model.

as follows:

$$f_{\mathrm{m}} = \sum_{i=1}^{n\gamma b} \frac{f_{\mathrm{m}_{\mathrm{cell}_i}}}{\mathrm{nc}} \tag{18}$$

$$f_{\gamma\mathrm{ret}} = 1 - (f_{\mathrm{Gr}} + f_{\mathrm{sh}} + f_{\mathrm{m}}) \tag{19}$$

where $n\gamma b$ is the number of austenite block cells.

Numerical implementation

The model was computationally implemented using Fortran language and the visualisation was performed with the Paraview software [31]. The differential equation (15) was solved by the implicit finite difference method using a grid with the same size as the employed for the CA model. A flow diagram of the resolution procedure is schematically shown in Figure 4. The required input data are the nominal chemical composition of ductile iron, the equilibrium segregation coefficients of alloy elements, the austenitisation and austempering temperatures, the austempering time (t_A), the number and size of graphite nodules, the graphite volume fraction, the constants k_a and k_m, the time step (Δt), and the cell side length or the number of cells employed to discretise the cubic domain.

Results and discussion

The influence of chemical composition on the developments of the ausferritic and martensitic transformations are analysed by taking into account both homogeneous and microsegregated distributions of alloy elements in austenite. The analysed chemical compositions correspond to an Fe–C–Si ductile iron, four mono-alloyed ductile irons with a high amount of Mn, Mo, Ni, or Cu, and two multi-alloyed ductile irons. Details of the nominal chemical compositions are presented in Table 1. In the analysis, the graphite volume fraction is $f_{\mathrm{Gr}} = 0.1$, the radii of equal size graphite nodules are varied in the range of 7–20 μm, the austenitisation and austempering temperatures are $T_\gamma = 1143$

Table 1. Nominal chemical compositions for the proposed ductile irons (alloy element concentrations in wt-%).

Alloy	W_{C_o}	W_{Si_o}	W_{Mn_o}	W_{Mo_o}	W_{Ni_o}	W_{Cu_o}
1	3.81	2.5	–	–	–	–
2	3.82	2.5	0.67	–	–	–
3	3.72	2.5	–	0.33	–	–
4	3.68	2.5	–	–	2	–
5	3.83	2.5	–	–	–	1
6	3.71	2.5	0.33	0.17	1	0.5
7	3.6	2.5	0.67	0.33	2	1

K (870° C) and $T_A = 648$ K (375° C), the cubic domain is discretised with $80 \times 80 \times 80$ cells, and the time step is $\Delta t = 5$ s. The number of cells for the spatial discretisation and the time step for the time discretisation were obtained by means of a convergence study. Moreover, the constant values $k_a = 1.30104 \times 10^{14}$ and $k_m = 6.6 \times 10^{-3}$ were obtained by fitting the model response to the experimental data presented in Ref. [32]. For each analysed case, the numerical representative volume element is obtained by the ensemble averaging procedure [33], for which 15 random realisations of a cubic domain with six graphite nodules are employed. For microsegregated distribution of alloy elements, the employed equilibrium segregation coefficients are $k_{Si} = 1.09$, $k_{Mn} = 0.7$, $k_{Mo} = 0.26$, $k_{Ni} = 1.23$, and $k_{Cu} = 1.37$, which were extracted from Ref. [34].

Alloy element distributions

The computed alloy element concentrations in austenite, for HD of alloy elements, are presented in Table 2. It is observed that these concentrations were higher than the nominal chemical composition.

For microsegregated distribution of alloy elements, the micro-constituents and Si distribution for different stages of the solidification process are presented in Figure 5 for alloy 2. Austenite grows with the shape of halos, which begin to be in contact with $f_{\gamma\mathrm{sol}_n} > 0.15$. The Si is uniformly distributed in the liquid and its concentration decreases with the increment of $f_{\gamma\mathrm{sol}_n}$. The FTF region is located close to graphite nodules and LTF region is located at intercellular boundaries with the largest distance to graphite nodules. The shape and position of the LTF region depend on the graphite nodule locations, which were randomly assigned.

Table 2. HD of alloy elements: computed alloy element concentrations, in wt-%, and initial value of $(\Delta Gm - Gn)$, in J mol^{-1}.

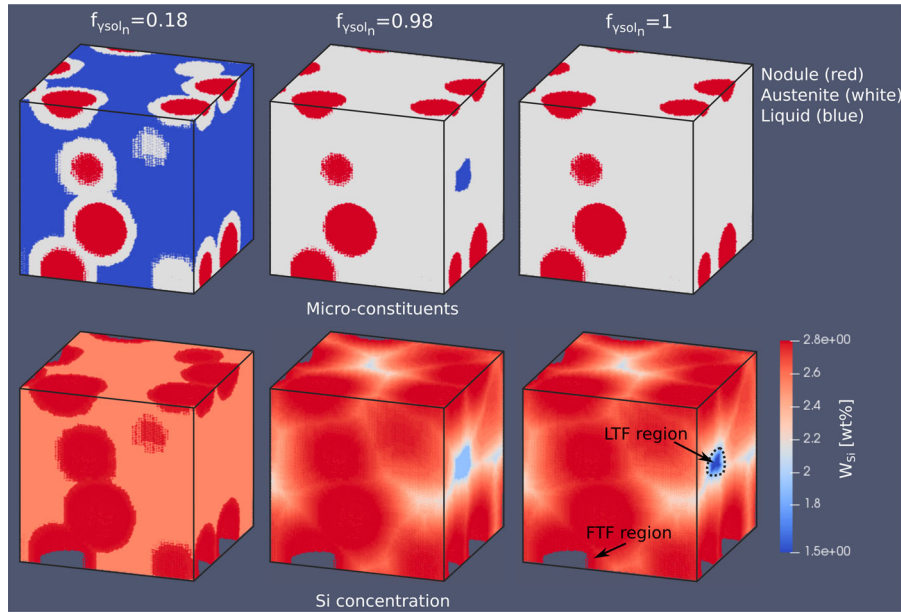| Alloy	W_{Si}	W_{Mn}	W_{Mo}	W_{Ni}	W_{Cu}	$(\Delta Gm - Gn)_o$
1	2.58	–	–	–	–	−655.98
2	2.58	0.69	–	–	–	−479.34
3	2.58	–	0.34	–	–	−671.41
4	2.58	–	–	2.06	–	−611.91
5	2.58	–	–	–	1.03	−610.66
6	2.58	0.34	0.18	1.03	0.52	−532.29
7	2.58	0.69	0.34	2.06	1.03	−401.07

Figure 5. Micro-constituents and Si distribution during the solidification for alloy 2. Graphite nodules are not included in the visualisation of Si concentration.

Table 3. Microsegregated distribution of alloy elements: computed alloy element concentrations, in wt-%, and initial value of $(\triangle Gm - Gn)$, in J mol^{-1}, at FTF and LTF regions.

Alloy	Region	W_{Si}	W_{Mn}	W_{Mo}	W_{Ni}	W_{Cu}	$(\triangle Gm - Gn)_o$
1	FTF	2.80	–	–	–	–	−649.55
	LTF	1.51	–	–	–	–	−686.5
2	FTF	2.80	0.49	–	–	–	−526.34
	LTF	1.51	3.84	–	–	–	263.79
3	FTF	2.80	–	0.09	–	–	−689.17
	LTF	1.51	–	14.68	–	–	770.08
4	FTF	2.80	–	–	2.51	–	−575.73
	LTF	1.51	–	–	0.52	–	−726.21
5	FTF	2.80	–	–	–	1.39	−590.91
	LTF	1.51	–	–	–	0.11	−675.15
6	FTF	2.80	0.24	0.05	1.26	0.70	−545.68
	LTF	1.51	1.89	7.56	0.26	0.06	601.06
7	FTF	2.80	0.49	0.09	2.51	1.39	−435.12
	LTF	1.51	3.84	14.68	0.52	0.11	892.37

The computed alloy concentrations in the matrix at FTF and LTF regions are presented in Table 3. As was reported in experimental works [6, 7], positive segregations were obtained with the model for Mn and Mo, and negative ones for Si, Cu, and Ni.

Owing to no diffusion of alloy elements at solid and perfect mixing at liquid were considered, the predicted segregation ratio (relation between alloy concentrations at LTF and FTF regions) did not depend on graphite nodule size or austenite halo growth rate during the solidification process. Moreover, as was studied in Ref. [23], the segregations of alloy elements obtained with the Scheil equation are more severe than those obtained by considering limited diffusion of alloy elements at solid and liquid phases. Despite these restrictions, in the presented work, two limit cases are studied: (a) HD of alloy elements and (b) severe microsegregated distribution of alloy elements. Employing microsegregation models with different hypotheses about the alloy element diffusion, the obtained results will be bounded by the results of these two limit cases.

Development of the ausferritic transformation

The evolution of phase volume fractions during the ausferritic transformation is presented in Figure 6 for alloy 1 with graphite nodules of $r_{Gr} = 20\,\mu m$. The ferrite platelet volume fraction increased with the time as a consequence of the nucleation and growth of ferrite platelets. On the other hand, the austenite volume fraction had an opposite behaviour because it was consumed by ferrite. The graphite volume fraction remained constant during the transformation.

Figure 7(a) presents the required austempering time $t_{A99.5}$ to get a ferrite platelet volume fraction equal to $0.995f_{\alpha p_{max}}$ for different graphite nodule sizes and taking into account a HD of alloy elements. For each alloy, $t_{A99.5(HD)}$ increased with the increment of graphite nodule size; this behaviour is in agreement with the experimental observations of Ref. [3]. This occurs because the nodule surface per
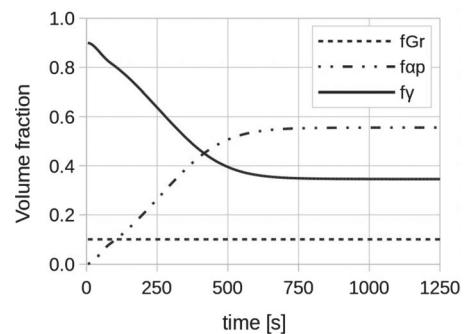

Figure 6. Phase fractions during the ausferritic transformation for alloy 1 with graphite nodules of $r_{Gr} = 20\,\mu m$.
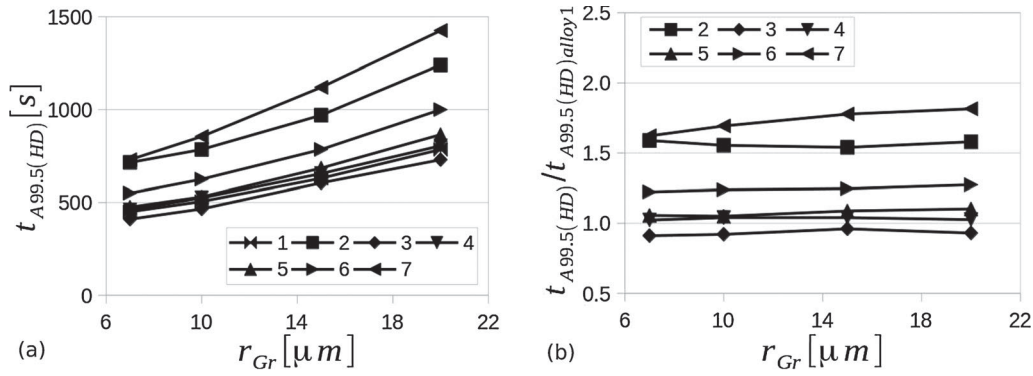
Figure 7. (a) Required austempering time to get a ferrite platelet volume fraction equal to $0.995 f_{\alpha p_{max}}$ and (b) relation between $t_{A99.5(HD)}$ and $t_{A99.5(HD)alloy1}$, both for a HD of alloy elements.

unit of volume decreased, and this in turn decreased the nucleation rate at the beginning of the transformation. Figure 7(b) presents the relation between $t_{A99.5(HD)}$ and $t_{A99.5(HD)alloy1}$ that allows measuring the delay/acceleration in the development of the transformation with respect to the alloy 1. It is observed that for mono-alloyed ductile irons the largest delay was obtained for a high amount of Mn (alloy 2). The Ni and Cu additions (alloys 4 and 5) produced a small delay, whereas the addition of Mo (alloy 3) produced a small acceleration. For the multi-alloyed ductile irons, the largest delay was obtained for high contents of alloy elements (alloy 7). The influence of alloy elements did not depend strongly on graphite nodule size.

The growth kinetics of ferrite platelets was modified by the microsegregations of alloy elements. During the first part of ausferritic transformation, the required austempering time to get a ferrite platelet volume fraction equal to $0.5 f_{\alpha p_{max}}$ (t_{A50}) was decreased by the microsegregations of Mn and Mo and increased by the microsegregations of Si, Ni, and Cu, as is observed in the relation between $t_{A50(MD)}$ and $t_{A50(HD)}$ presented in Figure 8(a). This occurred because close to FTF region (where the transformation begins) the low concentrations of Mn and Mo, due to their positive segregations, generated a $(\Delta Gm - Gn)$ smaller than for the HD as is shown in Tables 2 and 3, which increased the growth rate of ferrite platelets. On the other hand, the high concentrations of Si, Ni, and Cu close to FTF region, due to their negative segregations, generated a $(\Delta Gm - Gn)$ larger than for the HD that decreased the growth rate of ferrite platelets. As is
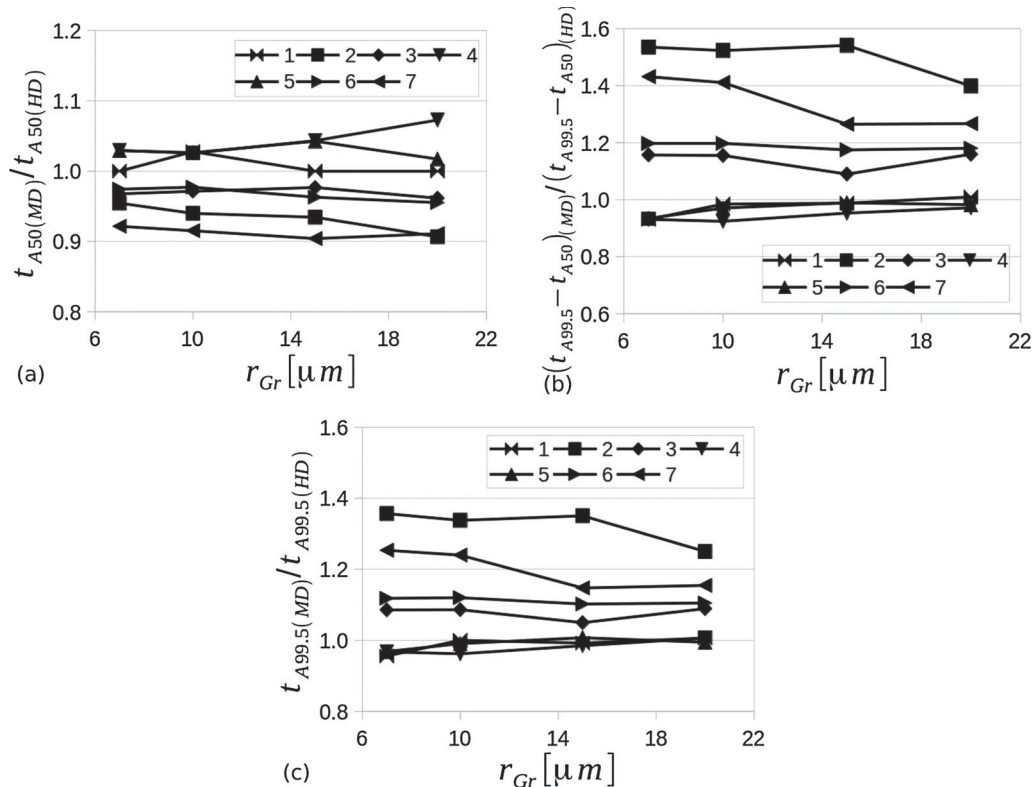

Figure 8. Relation between (a) $t_{A50(MD)}$ and $t_{A50(HD)}$, (b) $(t_{A99.5} - t_{A50})_{(MD)}$ and $(t_{A99.5} - t_{A50})_{(HD)}$, and (c) $t_{A99.5(MD)}$ and $t_{A99.5(HD)}$.

observed in Figure 8(b), during the last part of the aus-ferritic transformation the influence of alloy element microsegregations on ferrite platelet growth was opposite to the previously described. This occurred because close to LTF region the high/low concentrations of alloy elements with positive/negative segregations generate a $(\Delta Gm - Gn)$ larger/smaller than for the HD that decreased/increased the growth rate of ferrite platelets. The microsegregations of alloy elements slightly modified the first part of the transformation, whereas they strongly affected the last part especially when Mn and Mo were added. The overall effect of microsegregated distribution was an increment of $t_{A99.5}$ with respect to the homogeneous one, which is observed in the relation between $t_{A99.5(MD)}$ and $t_{A99.5(HD)}$ presented in Figure 8(c). The largest delay in the transformation (the largest value of $t_{A99.5(MD)}/t_{A99.5(HD)}$) was observed for ductile irons alloyed with Mn and Mo.

Figure 9(a) presents the ferrite platelet volume fraction at the end of the ausferritic transformation for a HD of alloy elements, as a function of the graphite nodule size. From the results of mono-alloyed ductile irons, it is observed that the addition of Mn reduced the final volume fraction, and the addition of Mo, Ni, and Cu increased it. The maximum volume fraction of ferrite platelets was obtained for the multi-alloyed ductile iron with high contents of all mentioned alloy elements (alloy 7). The computed volume fraction increased with the increment of the graphite nodule size because the cell size employed to discretise the cubic domain was increased. The increment of the cell size causes that the capture algorithm slightly increases the volume fraction of cells where the ausferritic transformation takes place. Figure 9(b) presents the relation between the final ferrite platelet volume fractions for microsegregated and HDs of alloy elements. A slight reduction in
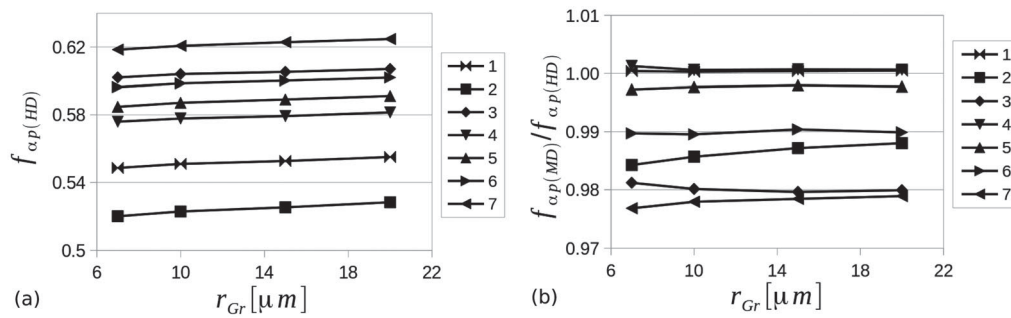

Figure 9. (a) Final ferrite platelet volume fraction for the HD and (b) relation between the final ferrite platelet volume fractions for microsegregated and HDs.
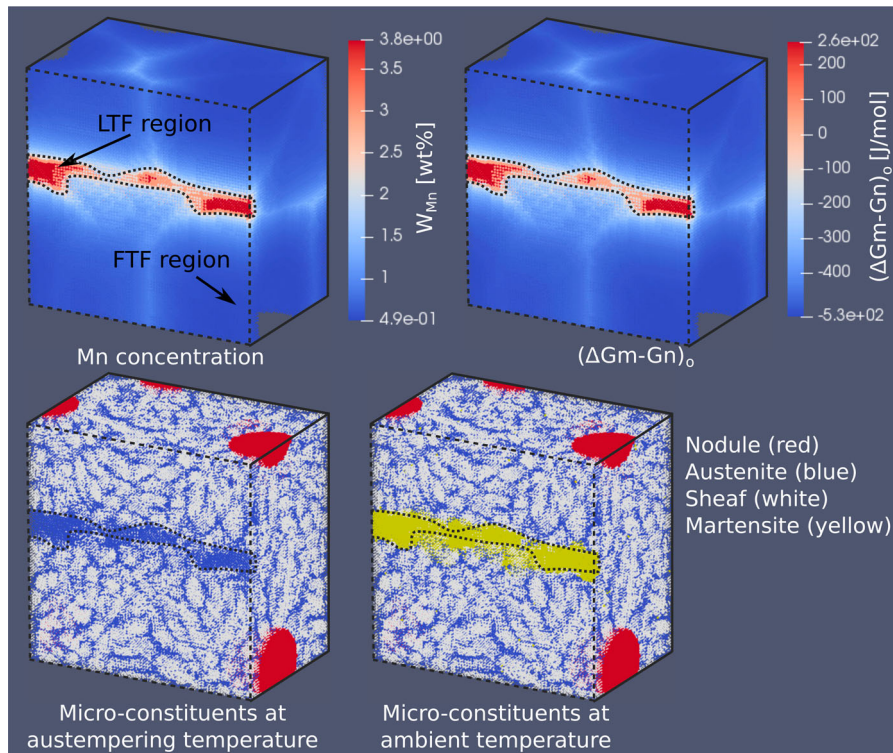

Figure 10. Mn distribution, initial value of $(\Delta Gm - Gn)$, and micro-constituents at the end of the ausferritic transformation, to austempering and ambient temperatures, for alloy 2. Graphite nodules are not included in the visualisations of Mn concentration and $(\Delta Gm - Gn)$ value.
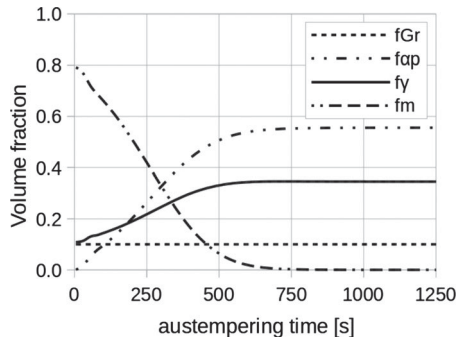
Figure 11. Phase fractions at ambient temperature, for different austempering times, for alloy 1 with graphite nodules of $r_{Gr} = 20\,\mu$m.

the volume fraction is observed for the microsegregated distribution, with respect to the homogeneous one, for alloys that have Mn and Mo. This reduction occurred because $(\Delta Gm - Gn) > 0$ at LTF region, see Table 3; therefore the austenite is not able to transform into ferrite platelets. In Figure 10, it is possible to observe the influence of Mn microsegregation in the initial value of $(\Delta Gm - Gn)$, which modifies the final microstructure especially at LTF region where sheaves were not formed.

Development of the martensitic transformation

During the cooling down from austempering temperature to ambient temperature (third step of the austempering heat treatment), the transformation of austenite into martensite depended on the austempering time. As is shown in Figure 11 for alloy 1 with graphite nodules of $r_{Gr} = 20\,\mu$m, for a short austempering time a small amount of austenite was retained at ambient temperature because a large amount of martensite was formed. This occurred because austenite with low carbon concentration was obtained during the ausferritic transformation, as a consequence of a small formation of ferrite platelets, causing a T_{MS} temperature higher than the ambient temperature. When the austempering time was increased, a bigger amount of ferrite platelets was formed increasing the austenite carbon concentration. For this reason, at ambient temperature more austenite was retained and less martensite was formed
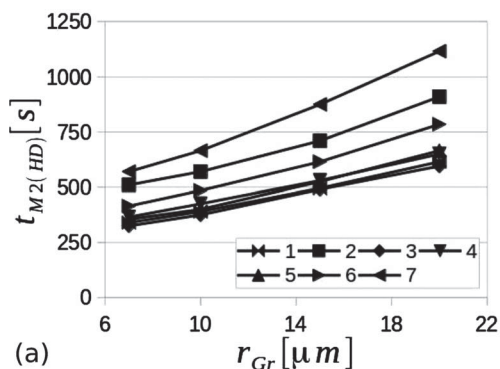
as a consequence of T_{MS} reduction. When the austenite carbon concentration is high enough, the austenite is completely retained at ambient temperature. When the ausferritic transformation ended, the austenite was completely retained at ambient temperature in the analysed cases with a HD of alloy elements. In contrast, for the microsegregated distribution of alloy elements, the alloys that contain Mn and Mo presented a small amount of martensite at LTF region, as is shown in Figure 10 for alloy 2.

Figure 12(a) presents the required austempering time t_{M2} to get a martensite volume fraction, after cooling down to ambient temperature, equal to 0.02 for different graphite nodule sizes and taking into account a HD of alloy elements. For each alloy, $t_{M2}(HD)$ increased with the increment of graphite nodule size. As was mentioned above, the austenite requires a high enough carbon concentration to be completely retained at ambient temperature, which is obtained from ferrite platelets that are formed during the ausferritic transformation. When the graphite nodule size increases, more austempering time is necessary to obtain the adequate ferrite platelet volume fraction that allows to retain all the austenite at ambient temperature. Figure 12(b) presents the relation between $t_{M2(HD)}$ and $t_{M2(HD)alloy1}$ that allows measuring the influence of alloy elements in t_{M2}. It is observed that for mono-alloyed ductile irons the largest increment was obtained for a high amount of Mn (alloy 2). The Ni and Cu additions (alloys 4 and 5) produced a small increment, whereas the
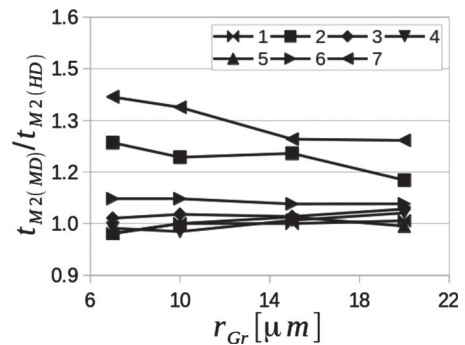

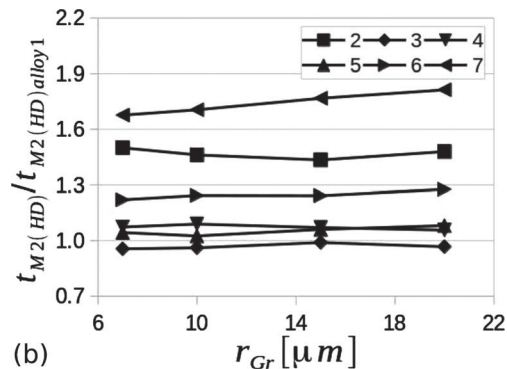**Figure 13.** Relation between $t_{M2(MD)}$ and $t_{M2(HD)}$.

Figure 12. (a) Required austempering time to get a martensite volume fraction equal to 0.02 and (b) relation between $t_{M2(HD)}$ and $t_{M2(HD)alloy1}$, both for a HD of alloy elements.

Table 4. Ductile iron characteristics of experimental samples extracted from Refs. [10, 32]. The nominal chemical composition is in wt-% and the nodule count is in nod mm^{-2}.

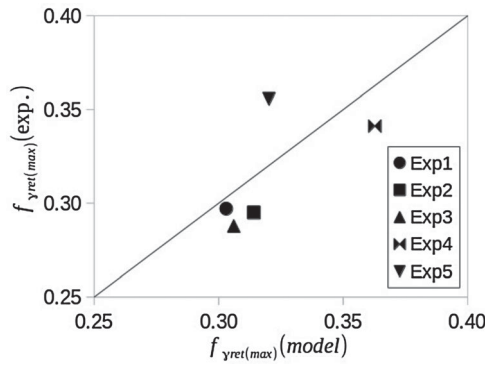| Alloy	W_{C_o}	W_{Si_o}	W_{Mn_o}	W_{Cu_o}	W_{Ni_o}	W_{Mo_o}	f_{Gr}	Nodule count
Exp1	3.39	2.56	0.37	0.29	–	0.25	0.117	104
Exp2	3.52	2.64	0.67	0.25	–	0.25	0.12	102
Exp3	3.5	2.32	0.59	0.29	–	0.33	0.121	230
Exp4	3.8	2.77	0.04	0.33	0.07	–	0.102	180
Exp5	3.6	2.8	0.02	0.9	1.02	–	0.092	66

Figure 14. Comparison of computed and measured maximum austenite volume fractions retained at ambient temperature.

addition of Mo (alloy 3) produced a small decrement. For the multi-alloyed ductile irons, the largest increment was obtained for high contents of alloy elements (alloy 7).

The overall effect of microsegregated distribution of alloy elements was an increment of t_{M2}, with respect to the homogeneous one, which is observed in the relation between $t_{M2(MD)}$ and $t_{M2(HD)}$ presented in Figure 13. A large increment of t_{M2} was observed for ductile irons with a high amount of Mn. Owing to the relation between t_{M2} and the development of the ausferritic transformation, t_{M2} and $t_{A99.5}$ are influenced in the same way with the variations of (a) ductile iron chemical composition and (b) alloy element distribution in austenite. Finally, for the studied cases t_{M2} is lower than $t_{A99.5}$.

Comparison with experimental data

The numerical results are compared with the experimental data extracted from Refs. [10, 32] corresponding to samples austenitised at $T_\gamma = 1143$ K (870°C) [32] and $T_\gamma = 1173$ K (900°C) [10], and austempered at $T_A = 643$ K (370°C) [10] and $T_A = 648$ K (375°C) [32]. The nominal chemical composition, graphite volume fraction, and graphite nodule count are presented
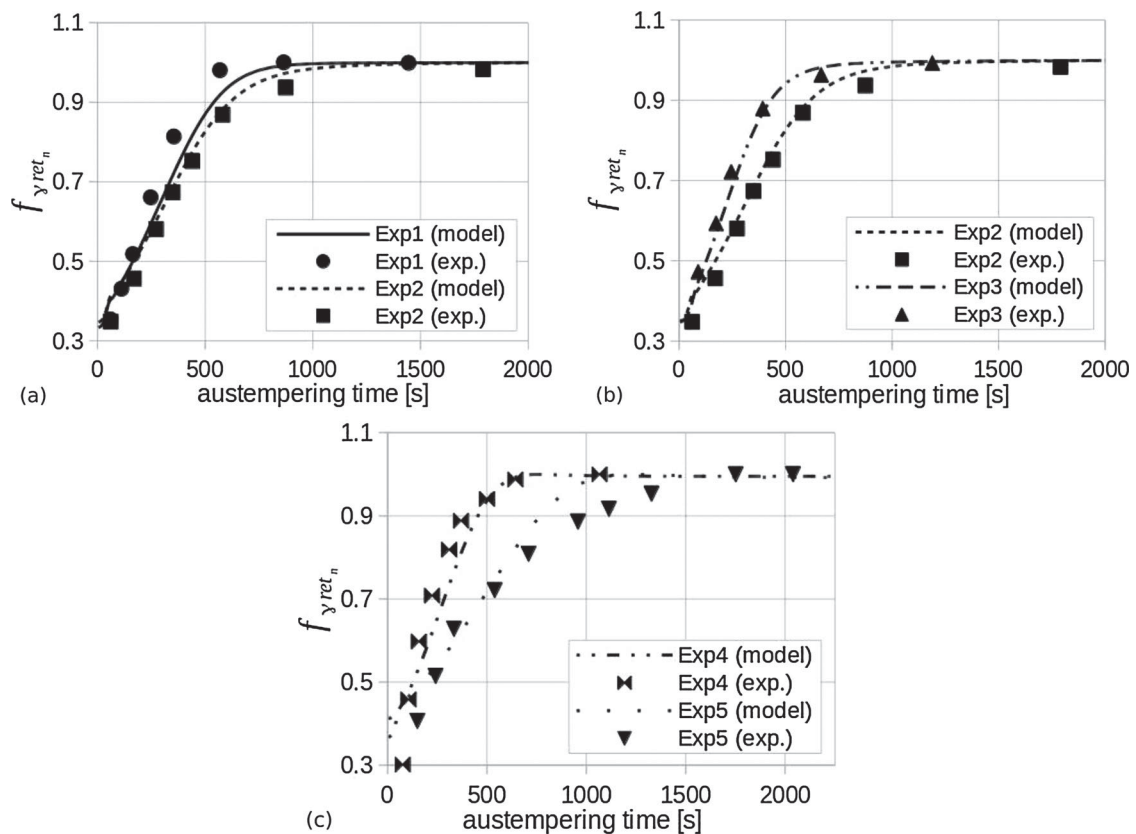

Figure 15. Comparison of computed and measured normalised austenite volume fractions, retained at ambient temperature, for the variations of (a) Mn content, (b) graphite nodule size, and (c) Ni–Cu content and graphite nodule size.

in Table 4. The samples are modelled taking into account a cubic domain with six graphite nodules of equal size and a microsegregated distribution of alloy elements in austenite. The results are obtained by employing 15 random realisations. The following input data are considered: $k_a = 1.30104 \times 10^{14}$, $k_m = 6.6 \times 10^{-3}$, cubic domain discretised with $80 \times 80 \times 80$ cells, and time step $\Delta t = 5$ s. As was mentioned above, the values of k_a and k_m were obtained by fitting the model response, and the number of cells and the time step were obtained by means of a convergence study.

Figure 14 compares the maximum austenite volume fractions, retained at ambient temperature, computed with the CA-FD model and measured from experiments. The obtained volume fractions were around 0.32. Figure 15 compares the computed and measured austenite volume fractions, retained at ambient temperature for different austempering times, normalised with respect to their maximum values ($f_{\gamma \mathrm{ret_n}}$). The influence of Mn content, graphite nodule size, and Ni–Cu content and graphite nodule size are observed in Figure 15(a), (b), and (c), respectively. A good correlation between the model and the experimental results was obtained.

According to the experimental results of Refs. [10, 32], the volume fraction of unreacted austenite was lesser or equal than 0.03 for the maximum austempering time. The unreacted austenite was located at LTF region and was partially transformed into martensite during the cooling down to ambient temperature. According to the model results, the volume fraction of austenite with low carbon concentration was lesser or equal than 0.02 and also was located at LTF region. This austenite was partially transformed into martensite during the cooling down to ambient temperature. The martensite volume fraction was lesser or equal than 0.01. Finally, the average austenite carbon concentration for the maximum austempering time was around 2 wt-% for both experimental and model results.

Conclusions

A CA-FD model was employed in this paper to analyse the influence of homogeneous and microsegregated distributions of alloy elements on ADI microstructure and its heat treatment. The main conclusions of this work may be summarised as follows:

(1) The model allows predicting the microsegregations of alloy elements according to the unicellular solidification theory. The microsegregated distribution of alloy elements presents a positive segregation for Mn and Mo, and a negative one for Si, Cu, and Ni. The shape and position of the LTF region depend on the graphite nodule positions in the matrix. Owing to the adoption of the Scheil equation, severe segregations of alloy elements are obtained.

(2) For ductile irons alloyed with Mn and Mo, the final volume fraction of ferrite platelets for the microsegregated distribution of alloy elements is smaller than for the homogeneous one. The LTF region takes a key role in the resulting fractions for the microsegregated distribution, because the thermodynamic criterion to transform austenite into ferrite platelets is not satisfied in this region.

(3) The kinetics of ausferritic transformation for both distributions of alloy elements is highly modified by the graphite nodule size. An increment in the graphite nodule size decreases the transformation rate. When microsegregated distribution of alloy elements is considered, the transformation spends more time to be completed, especially for alloys with high contents of Mn and Mo that present an increment up to $\approx 30\%$ with respect to the HD.

(4) The martensitic transformation takes place during the cooling down to ambient temperature when short austempering times are employed. This modifies the volume fraction of retained austenite at ambient temperature, which increases with an austempering time increment. For both distributions of alloy elements, the required austempering time to obtained a martensite volume fraction, at ambient temperature, equal to 0.02 increases with the graphite nodules size and the addition of alloy elements such as Mn. Moreover, the computed retained austenite volume fraction at ambient temperature for different chemical compositions and different graphite nodule sizes is in a fairly good agreement with the experimental data reported in the literature.

(5) The results obtained with the proposed homogeneous and microsegregated alloy element distributions constitute limit cases, therefore using other microsegregation models, such as that of Ref. [23], an intermediate response will be reached. According to Refs. [6, 7, 11], the distribution of alloy elements in samples with high graphite nodule count trends to be homogeneous, and in those with low graphite nodule count trends to be strongly segregated. For this reason, the results obtained with the model taking into account a HD may yield a better representation for ductile irons with high graphite nodule count, whereas those obtained by taking into account a microsegregated distribution may lead to a better representation for ductile irons with low graphite nodule count.

Disclosure statement

Funding

ORCID

A. D. Boccardo http://orcid.org/0000-0003-3299-2510
P. M. Dardati http://orcid.org/0000-0002-3294-2962

References

[1] Bhadeshia HKDH. Bainite in steels. 2nd ed. London: IOM Communications; 2001.

[2] Chang LC. An analysis of retained austenite in austempered ductile iron. Mater Trans A. 2003;34(2):211–217.

[3] Fraś E, Górny M, Tyrała E, et al. Effect of nodule count on austenitising and austempering kinetics of ductile iron castings and mechanical properties of thin walled iron castings. Mater Sci Technol. 2012;28(12):1391–1396.

[4] Thomson RC, James JS, Putman DC. Modelling microstructural evolution and mechanical properties of austempered ductile iron. Mater Sci Technol. 2000;16(11–12):1412–1419.

[5] Yescas MA, Bhadeshia HKDH. Model for the maximum fraction of retained austenite in austempered ductile cast iron. Mater Sci Eng A. 2002;333(1–2):60–66.

[6] Lin BY, Chen ET, Lei TS. The effect of segregation on the austemper transformation and toughness of ductile iron. J Mater Eng Perform. 1998;7(3):407–419.

[7] Liu J, Elliott R. The influence of cast structure on the austempering of ductile iron, part 1: modelling of the influence of nodule count on microsegregation. Int J Cast Met Res. 1998;10(6):301–305.

[8] Bosnjak B, Radulovic B, Pop-Tonev K, et al. Influence of microalloying and heat treatment on the kinetics of bainitic reaction in austempered ductile iron. J Mater Eng Perform. 2001;10(2):203–211.

[9] Liu J, Elliott R. The influence of cast structure on the austempering of ductile iron, part 2: assessment of model calculations of microsegregation. Int J Cast Met Res. 1999;12(2):75–82.

[10] Darwish N, Elliott R. Austempering of low manganese ductile irons. Mater Sci Technol. 1993;9(7):572–585.

[11] Akbarzadeh Chiniforush E, Iranipour N, Yazdani S. Effect of nodule count and austempering heat treatment on segregation behavior of alloying elements in ductile cast iron. China Foundry. 2016;13(3):217–222.

[12] Sheikholeslam A, Nili Ahmadabadi M, Rassizadehghani J. The effect of partial melting homogenization on the mechanical properties of thick section austempered ductile iron containing 2% Mn. Key Eng Mater. 2011;457:193–198.

[13] Rahgozar N, Nili-Ahmadabadi M, Forghani F. Development of high Mo carbide free thick section nodular cast iron by partial melting homogenisation. Mater Sci Technol. 2013;29(11):1346–1353.

[14] Kapturkiewicz W, Burbelko AA, Lelito J, et al. Modelling of ausferrite growth in ADI. Int J Cast Met Res. 2003;16(1–3):287–292.

[15] Hepp E, Hurevich V, Schäfer W. Integrated modeling and heat treatment simulation of austempered ductile iron. IOP Conf Ser: Mater Sci Eng. 2012;33(1):012076.

[16] Boccardo AD, Dardati PM, Celentano DJ, et al. A microscale model for ausferritic transformation of austempered ductile irons. Mater Trans A. 2017;48(1):524–535.

[17] Boccardo AD, Dardati PM, Godoy LA. A cellular automaton-finite difference simulation of the ausferritic transformation in ductile iron. Mater Sci Technol. 2018. Available from: https://doi.org/10.1080/02670836.2018.1475035.

[18] Scheil E. Bemerkungen zur schichtkristallbildung [Remarks on the crystal layer formation]. Z Metallk. 1942;34:70–72.

[19] Putman DC, Thomson RC. Microstructural and mechanical property modelling of austempered ductile iron. Int J Cast Met Res. 2003;16(1–3):191–196.

[20] Sieradzki L, Madej L. A perceptive comparison of the cellular automata and Monte Carlo techniques in application to static recrystallization modeling in polycrystalline materials. Comput Mater Sci. 2013;67:156–173.

[21] Rintoul MD, Torquato S. Reconstruction of the structure of dispersions. J Colloid Interface Sci. 1997;186(2):467–476.

[22] Lacaze J, Gerval V. Modelling of the eutectoid reaction in spheroidal graphite Fe–C–Si alloys. ISIJ Int. 1998;38(7):714–722.

[23] Liu J, Elliott R. Numerical model for microsegregation in ductile iron. Mater Sci Technol. 1998;14(11):1127–1131.

[24] Rees GI, Bhadeshia HKDH. Bainite transformation kinetics, part 1: modified model. Mater Sci Technol. 1992;8(11):985–993.

[25] Matsuda H, Bhadeshia HKDH. Kinetics of the bainite transformation. Proc R Soc Lond A. 2004;460(2046):1707–1722.

[26] Gaude-Fugarolas D, Jacques PJ. A new physical model for the kinetics of the bainite transformation. ISIJ Int. 2006;46(5):712–717.

[27] Bhadeshia HKDH. Thermodynamic analysis of isothermal transformation diagrams. Metal Sci. 1982;16(3):159–166.

[28] Ågren J. A revised expression for the diffusivity of carbon in binary Fe-C austenite. Scr Mater. 1986;20(11):1507–1510.

[29] Khan SA, Bhadeshia HKDH. Kinetics of martensite transformation in partially bainitic 300M Steel. Mater Sci Eng A. 1990;129(2):257–272.

[30] Nehrenberg AE. Technical publication 2059: discussion, iron and steel division. Met Technol (N Y). 1946;XIII:33–43. Available from: http://library.aimehq.org/library/metals-technology-1946-vol-xiii.html.

[31] Ayachit U. The paraview guide: a parallel visualization application. New York: Kitware; 2015.

[32] Liu J, Elliott R. The influence of cast structure on the austempering of ductile iron, part 3: the role of nodule count on the kinetics, microstructure and mechanical properties of austempered Mn alloyed ductile iron. Int J Cast Met Res. 1999;12(3):189–195.

[33] Temizer I. Micromechanics: analysis of heterogeneous materials. Turkey: Department of Mechanical Engineering, Bilkent University; 2012. Available from: https://sourceforge.net/projects/multiscale.

[34] Boeri R, Weinberg F. Microsegregation in ductile iron. AFS Trans. 1989;97:179–184.